Analysis of posterior retinal layers in spectral optical coherence tomography images of the normal retina and retinal pathologies

Citation: Szkulmowski, Maciej, Maciej Wojtkowski, Bartosz Sikorski, Tomasz Bajraszewski, Vivek J. Srinivasan, Anna Szkulmowska, Jakub J. Kaluzny, James G. Fujimoto, and Andrzej Kowalczyk. "Analysis of Posterior Retinal Layers in Spectral Optical Coherence Tomography Images of the Normal Retina and Retinal Pathologies." Journal of Biomedical Optics 12, no. 4 (2007): 041207. © 2007 Society of Photo-Optical Instrumentation Engineers

As Published: http://dx.doi.org/10.1117/1.2771569

Publisher: SPIE

Persistent URL: http://hdl.handle.net/1721.1/87655

Version: Final published version: final published article, as it appeared in a journal, conference proceedings, or other formally published context

Journal of Biomedical Optics 12(4), 041207 (July/August 2007)

Analysis of posterior retinal layers in spectral optical coherence tomography images of the normal retina and retinal pathologies

Maciej Szkulmowski
Maciej Wojtkowski
Nicolaus Copernicus University
Institute of Physics
ul. Grudziądzka 5/7
PL-87-100 Toruń, Poland

Bartosz Sikorski
Nicolaus Copernicus University
Collegium Medicum
Department of Ophthalmology
Curie-Sklodowskiej 9
PL-85-094 Bydgoszcz, Poland

Tomasz Bajraszewski
Nicolaus Copernicus University
Institute of Physics
ul. Grudziądzka 5/7
PL-87-100 Toruń, Poland

Vivek J. Srinivasan
Massachusetts Institute of Technology
Department of Electrical Engineering and Computer Science
Research Laboratory of Electronics
Cambridge, Massachusetts 02139

Anna Szkulmowska
Nicolaus Copernicus University
Institute of Physics
ul. Grudziądzka 5/7
PL-87-100 Toruń, Poland

Jakub J. Kałużny
Nicolaus Copernicus University
Collegium Medicum
Department of Ophthalmology
Curie-Sklodowskiej 9
PL-85-094 Bydgoszcz, Poland

James G. Fujimoto
Massachusetts Institute of Technology
Department of Electrical Engineering and Computer Science
Research Laboratory of Electronics
Cambridge, Massachusetts 02139

Andrzej Kowalczyk
Nicolaus Copernicus University
Institute of Physics
ul. Grudziądzka 5/7
PL-87-100 Toruń, Poland

Abstract. We present a computationally efficient, semiautomated method for analysis of posterior retinal layers in three-dimensional (3-D) images obtained by spectral optical coherence tomography (SOCT). The method consists of two steps: segmentation of posterior retinal layers and analysis of their thickness and distance from an outer retinal contour (ORC), which is introduced to approximate the normal position of external interface of the healthy retinal pigment epithelium (RPE). The algorithm is shown to effectively segment posterior retina by classifying every pixel in the SOCT tomogram using the similarity of its surroundings to a reference set of model pixels from user-selected area(s). Operator intervention is required to assess the quality of segmentation. Thickness and distance maps from the segmented layers and their analysis are presented for healthy and pathological retinas. [DOI: 10.1117/1.2771569]

Keywords: optical coherence tomography (OCT); spectral optical coherence tomography (SOCT); image segmentation; image analysis.

Paper 06289SSRR received Oct. 13, 2006; revised manuscript received Apr. 25, 2007; accepted for publication Apr. 30, 2007; published online Aug. 17, 2007.

1 Introduction

Spectral optical coherence tomography (SOCT) is a novel embodiment of optical coherence tomography (OCT) that enables high-speed and high-resolution cross-sectional *in vivo* imaging of biological tissues.[1–3] In SOCT, the axial structure of an object (optical A-scan) is retrieved from the interferometric signal (spectral fringes) detected as a function of optical frequency. Because it has increased speed and sensitivity in comparison with standard time domain OCT, SOCT can be used for *in vivo* measurement of the three-dimensional (3-D)

Address all correspondence to Maciej Wojtkowski, Nicolaus Copernicus University, Institute of Physics, ul. Grudziądzka 5/7, PL-87-100 Toruń, Poland; Tel: 48–56–611–32–13; Fax: 48–56–622–53–97; E-mail: max@fizyka.umk.pl

1083-3668/2007/12(4)/041207/11/$25.00 © 2007 SPIE

structure of a measured object. SOCT, like previous OCT techniques, can provide noninvasive, micron-scale resolution imaging and is especially useful in ophthalmology for cross-sectional imaging of the anterior and posterior segments of the human eye.[4–15] In addition, because of its unique combination of both 3-D imaging capability and high axial resolution, SOCT is a very sensitive tool for the detection and monitoring of early pathological and morphological changes.

The retinal cross-sectional images measured by OCT instruments consist of alternately bright and dark layers because of the different backscattering properties of cells distributed in different morphological layers in the retina. It has been shown that there is a correlation between layers visible in histology and layers of different intensities visible in OCT cross-sectional images.[16–19] It must be noted, however, that histology displays structures with different staining properties, whereas OCT distinguishes structures with different backscattering intensity (reflectivity). Therefore, the correlation between these two methods is sometimes indirect. The current interpretation of OCT retinal images assumes that the strongest scattering layers are the nerve fiber layer (NFL) and the retinal pigment epithelium (RPE).[6,18] The most highly scattering part of the photoreceptor layer is visible in OCT images as a narrow line just above the RPE and is commonly assigned to the junction between the inner and outer segments of the photoreceptors—IS/OS junction.[19] The region bounded on one side by the IS/OS junction and on the other by the RPE outer boundary is very well visualized by ultrahigh-resolution OCT devices.[8] Because most retinal diseases affecting photoreceptors start in this area, we believe that higher-resolution analysis of this region should provide new, clinically valuable information.

The 3-D data provided by OCT can be presented in the form of retinal thickness maps. These promise to be very useful for diagnosis, because they instantly provide comprehensive information on the status of the retina, which correlates with the ophthalmoscopic view of the fundus.[6,7] Early pathological changes involving the photoreceptor layer, however, may not affect the overall thickness of the retina, and therefore early disease may not be detectable by total retinal thickness maps alone. These pathologies might be more easily detected if just the outer layers of the retina were to be imaged and analyzed.

The optical properties of the outer segment of the retina give rise to relatively strong OCT signals. However, in order to effectively perform segmentation and construct thickness maps of a specific retinal layer, the tomograms should be high resolution, have high transverse density axial scans, and be free of motion artifacts. SOCT has a significant advantage over previous OCT techniques and can acquire tomograms with reduced motion artifacts in patients because of its increased speed and sensitivity. Despite these favorable circumstances, improved methods of image analysis are needed, because SOCT images still have relatively low contrast, with diffuse, grainy structures and—in the case of pathologies—considerable irregularities and discontinuities.

A method of measuring the thickness of the entire retina and of the NFL thickness is incorporated in the software of commercially available OCT instruments, but these algorithms have not been precisely described in the literature. In general, these algorithms provide good repeatability,[20] but for some cases yield incorrect results.[20,21] This occurs more frequently in cases of decreased backscattering intensity or if there are discontinuities in a layered structure due to motion artifacts. This problem is substantially reduced using the algorithm proposed by Koozekanani et al.[21] These authors presented a boundary-detection method, which uses a one-dimensional (1-D) edge-detection kernel to yield edge primitives that are rated, selected, and organized to form a coherent boundary structure using a Markov model of the retinal boundary. The detection of retinal layer boundaries has also been addressed by many other researchers.[22–25] Ishikawa et al.[22] demonstrated a method to identify boundaries between four retinal layers by searching for abrupt changes in image intensity. The tomogram is median filtered, the retinal layers flattened before assessing the boundaries, and assumptions must be made about the sequence of retinal layers. A very similar approach was proposed by Fernandez et al.,[23] who applied a complex diffusion filter to the tomogram in order to remove speckle noise without blurring retinal structures. Their procedure searches for edges in a map obtained by calculating the first derivative of the structure coherence matrix using the denoised image. In this approach, similar assumptions about the retinal structure must be adopted. However, in the case of severe pathological disruption of the normal retinal structure, there are limitations in the algorithm performance. A different approach to the problem of segmentation of retinal layers was proposed by Fernandez et al.,[24] where the authors focus only on delineating fluid-filled regions in the retina. Their algorithm reduces speckle noise with the aid of an anisotropic diffusion filter and uses a deformable model to outline the contours of lesions. The deformable model was also used by Mujat et al.[25] to assess the thickness of the NFL. This algorithm also uses anisotropic noise removal prior to the segmentation process.

In all cases, the preceding algorithms reveal interfaces between retinal layers that differ in intensity or texture. Assumptions about the retina structure (such as continuity of layers ensuring that, e.g., the *n*th layer from the top is the same one throughout the whole cross section[22]) allow the researchers to assign abrupt changes in intensity to interfaces between layers. These approaches are all more accurate in the healthy retinas and those where only the thinning of the layers occurs due to pathology and are still vulnerable to the presence of discontinuities in the tomogram caused either by complete atrophy, detachment of retinal layers, or shifts in the image caused by eye movements.

In this manuscript, we present a segmentation method that is resistant to discontinuities in the tomogram. Our method requires operator guidance to assess the quality of segmentation in intermediate stages of the whole segmentation process. The segmentation recognizes layers in the tomogram that have similar brightness and texture. The segmented layers may therefore be even detached, broken, or composed with many separate parts. We demonstrate this segmentation approach using SOCT data for the outer retina, containing regions characterized by the high intensity of SOCT signal. In the normal case, those regions consist of two strongly reflective layers. The anterior part of the segmented ensemble of retinal layers corresponds roughly to the junction between the inner and outer segments of the photoreceptor layer (IS/OS), while the posterior part corresponds to the basement membrane of the RPE. In pathologic cases, the highly reflecting segmented area can also include scars, regions of fibrosis, exudates, or deposits. We propose a novel approach for analysis of such segmented layers by using an additional reference surface, formed by a set of outer retinal contours (ORCs). In an ideal case, the ORC corresponds indirectly to the position of Bruch's membrane of a normal, healthy retina. We also introduce three contour maps displaying the mutual distances between the IS/OS junction, RPE, and ORC. We show that these maps provide complementary information, which may be helpful for the diagnosis of retinal disease, especially in the macular region.

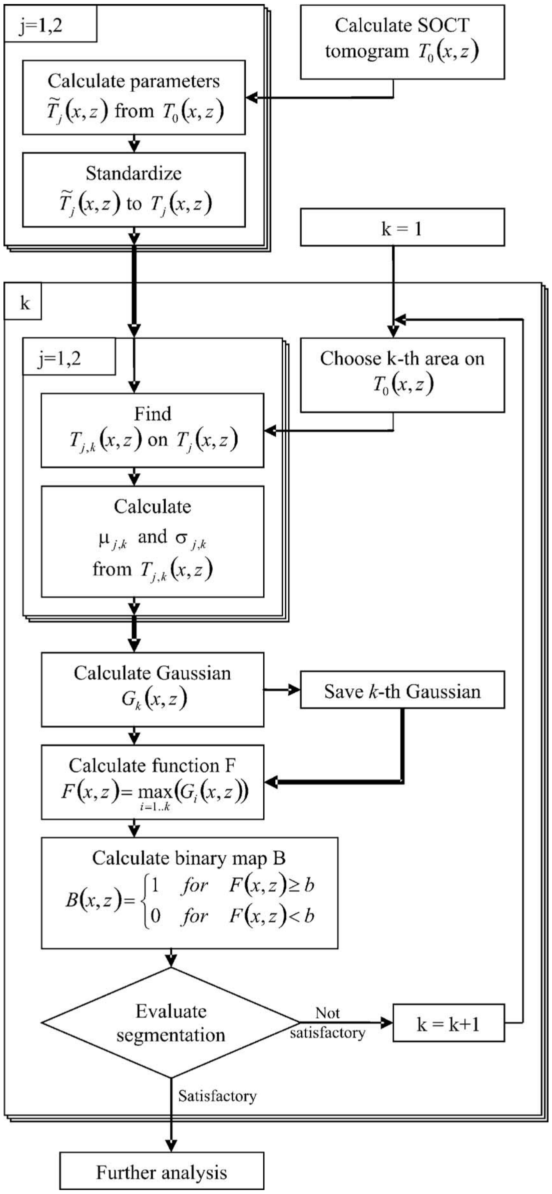

Fig. 1 Flow diagram of the segmentation algorithm. Details given in text.

2 Methods

The intensity of pixels in cross-sectional OCT images depends on the degree of heterogeneity of the tissue imaged, which in turn depends on the organization, size, orientation, and shape of the cells composing the tissue. Variation of intensity in retinal cross-sectional OCT images enables us to distinguish several layers, which are correlated with the real tissue structure.[19] In contrast to other methods used in OCT, where the interfaces between layers are sought, we apply a method that is a variation of a multiple thresholding algorithm used in segmentation tasks for image analysis.[26] The fundamental concept behind the algorithm is the assumption that both the mean intensity and variance calculated in the neighborhood of each pixel are similar for pixels belonging to a specific retinal layer. We calculate the two parameters for every pixel in its surrounding and analyze the position of the pixels in space defined by these parameters.

In the following subsections, we first present the algorithm, which with some operator intervention, enables segmentation of pixels having similar properties. In Sec. 2.2, we demonstrate that the entire numerical procedure enables segmentation and analysis of the highly scattering posterior retinal layers comprising the RPE and IS/OS junction. This semiautomated procedure uses the segmentation algorithm twice, first applying it coarsely to find the ORC, and in the second step applying it to flattened and cropped cross-sectional images, yielding a precise reconstruction of the posterior retinal layers.

2.1 *Segmentation Algorithm*

SOCT tomogram can be represented as a matrix of pixels T_0 (x, z). Coordinates $x=1,\ldots,N_x$ and $z=1,\ldots,N_z$ number, respectively, A-scans and pixels along each A-scan. The segmentation algorithm (Fig. 1) first calculates the values of two parameters: the weighted mean intensity $\tilde{T}_1(x,z)$ and its variance $\tilde{T}_2(x,z)$ for all pixels in the image. The parameters for a given pixel are calculated in its neighborhood by convolution with a Gaussian kernel $G(x,z)$:

$$\tilde{T}_1(x,z) = T_0(x,z) \otimes G(x,z), \tag{1}$$

$$\tilde{T}_2(x,z) = [\tilde{T}_1(x,z) - T_0(x,z)]^2 \otimes G(x,z). \tag{2}$$

The symbol $\otimes$ denotes convolution. The convolution is calculated via fast Fourier transformation (FFT) so that the Gaussian kernel $G(x,z)$ has the following form:

$$G(x_{\mathrm{mod}\,Nx}, z_{\mathrm{mod}\,Nz}) = \frac{1}{2\pi\sigma_x\sigma_z}\exp\left(-\frac{x^2}{2\sigma_x^2}\right)\exp\left(-\frac{z^2}{2\sigma_z^2}\right), \tag{3}$$

(in this case, $x=-N_x/2-1,\ldots,N_x/2$ and $z=-N_z/2-1,\ldots,N_z/2$). The parameters σ_x and σ_z determine the effective size of the kernel. The optimal values of σ_x and σ_z are chosen experimentally by the operator and kept constant for images obtained with the same instrument and measurement protocol. It is necessary to scale the two parameters $\tilde{T}_1(x,z)$ and $\tilde{T}_2(x,z)$ to have unit standard deviation and zero mean:

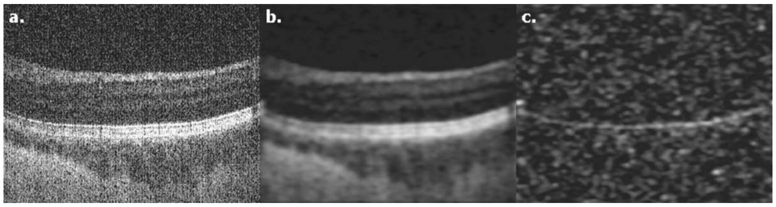

Fig. 2 (a) Map of intensity $T_0(x,z)$; (b) mean value of intensity $T_1(x,z)$; and (c) variance of intensity $T_2(x,z)$.

$$T_j(x,z) = \frac{\widetilde{T}_j(x,z) - \mu_j}{\sigma_j}, \qquad (4)$$

where μ_j is the mean, and σ_j the standard deviation, of $\widetilde{T}_j(x,z)$ ($j=1$, 2 throughout all the contribution). Figure 2 presents maps of $T_j(x,z)$ together with the original tomogram $T_0(x,z)$.

The algorithm considers the constructed values of the parameters $T_j(x,z)$ to be coordinates of the pixels in "parameter space" [Fig. 3(a)]. For the sake of clarity, we define "pixel" to be a pixel of the SOCT tomogram, and 'point' to be the representation of the pixel in the parameter space [determined by the coordinates $T_j(x,z)$].

In order to determine the boundaries in the distribution that enclose points corresponding to a certain retinal layer, the algorithm requires operator intervention. The operator has to choose in the tomogram a region of interest (ROI) that encloses a representative sample of pixels from the layer of interest.

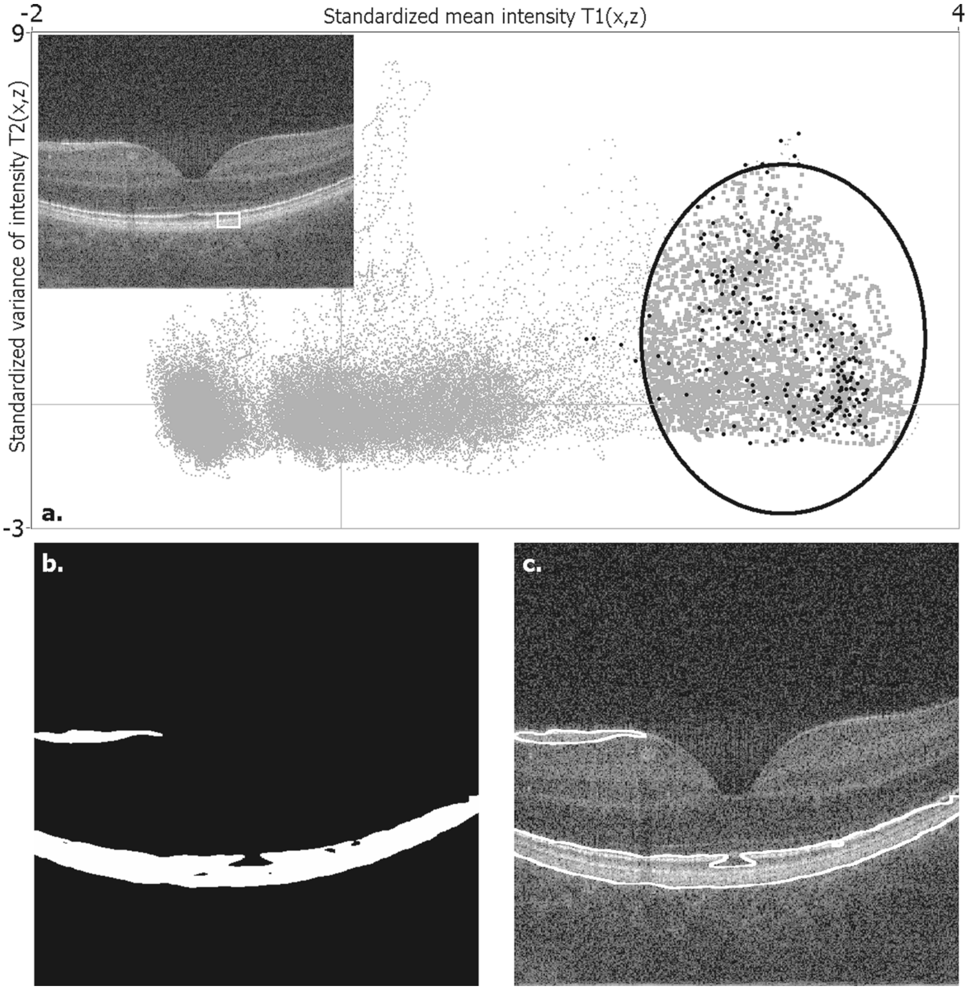

Fig. 3 Illustration of representative steps of the segmentation algorithm after selection of an ROI. (a) Points (black circles) corresponding to the selected ROI (white rectangle on the inset) superimposed on all points of the tomogram (gray points). The black ellipse delimits the area where the value of the function $F(x,z)$ is greater than 0.05. Points enclosed by the ellipse (gray squares) are considered to belong to the layer. (b) Binary map $B(x,z)$ created with points enclosed by the ellipse. (c) Edges of the binary map superimposed on the tomogram.

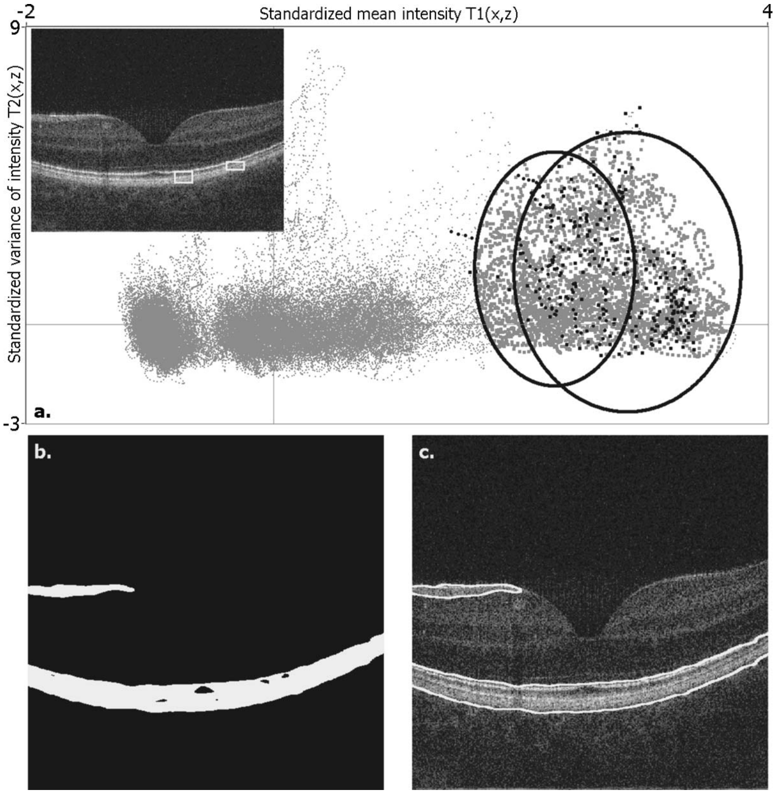

Fig. 4 Illustration of representative steps of the segmentation algorithm after selection of two ROIs. (a) Points (black circles) corresponding to the selected ROIs (white rectangles on the inset) superimposed on all points of the tomogram (gray points). The black ellipses delimit the area where the value of the functions $F(x,z)$ is greater than 0.05. Points enclosed by the ellipses (gray squares) are considered to belong to the layer. (b) Binary map $B(x,z)$ created with points enclosed by the ellipses. (c) Edges of the binary map superimposed on the tomogram.

The selection of the sample representative of a given layer in parameter space is equivalent to the choice of points that are localized in a single cluster [Fig. 3(a)]. The coordinates of points from the kth ROI chosen are noted as $T_{j,k}(x,z)$. In the next step, an estimate of the position of the center of gravity $\mu_{j,k}$ and the size of the cluster $\sigma_{j,k}$ is derived from the values of the samples $T_{j,k}(x,z)$ chosen. We approximate the density of points in the cluster by a Gaussian function $G_k(x,z)$:

$$G_k(x,z) = \exp\left\{ -\sum_j \left[\frac{T_j(x,z) - \mu_{j,k}}{\sqrt{2}\sigma_{j,k}} \right]^2 \right\}. \tag{5}$$

If the assumption that the density of points can be approximated by a Gaussian, for a single ROI, a value of $G_k(x,z)$ greater than 0.05 includes more than 99% of the points defined by the ROI [Fig. 3(a)].

When using multiple ROIs, the selected region in parameter space is constructed from more than one Gaussian function [Fig. 4(a)]. In such a reconstruction, the largest of the values of overlapping Gaussian functions is used, and a new function $F(x,z)$ is constructed:

$$F(x,z) = \max_{i=1..k}[G_i(x,z)]. \tag{6}$$

The algorithm assigns pixels to the layer if the value of the function $F(x,z)$ is greater than a defined threshold, b (for example, 0.05). This operation creates the binary map $B(x,z)$ defined by [Figs. 3(b) and 4(b)]:

$$B(x,z) = \begin{cases} 1 & \text{for } F(x,z) \geqslant b \\ 0 & \text{for } F(x,z) < b \end{cases}. \tag{7}$$

The standard edge detection algorithm, such as Robert's edge detector,[27] can now easily be applied to find the borders of the segmented layer. At this stage, the operator assesses the segmentation performance [Figs. 3(c) and 4(c)]. If the result is not satisfactory, the operator can replace, or add another, $(k+1)$th, ROI from a different part of the layer and construct a new $F(x,z)$ and new $B(x,z)$. If all parts of the segmented layer have similar parameters, then a single ROI is enough to define the cluster of all points in the layer for the entire 3-D set of data.

2.2 *Segmentation of Outer Retinal Layers*

Our procedure for analysis of the posterior highly scattering retinal layers is shown schematically in Fig. 5. We propose using the segmentation algorithm twice: first coarsely to find the ORC, and then a second, finer iteration performed on flattened and cropped cross-sectional images. During the initial step, the algorithm finds the posterior retinal layers at low resolution [Fig. 5(a) and 5(b)], which is assured by use of large sigmas Eqs. (1)–(3). The edge in the binary map $B(x,z)$, which is found automatically by searching from the choroid, is assigned as the posterior edge of the RPE.

The ORC, which will further serve as a reference [Fig. 5(c)], is found automatically by a weighted parabolic fitting to the posterior edge of RPE. The weights are proportional to the

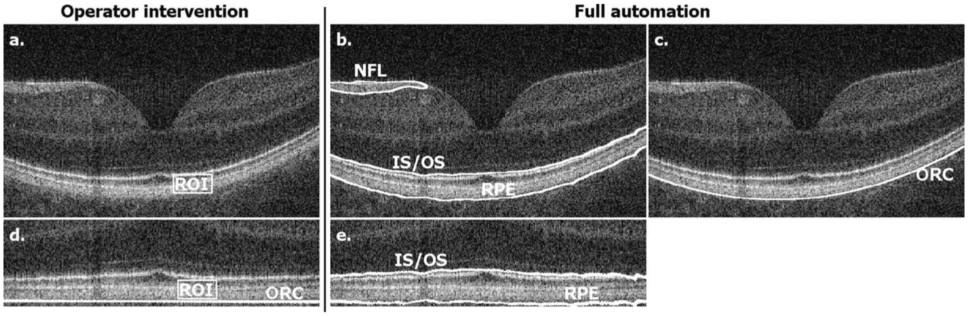

Fig. 5 Illustration of the procedure of segmentation of the posterior retinal layers including RPE and IS/OS junction. (a) to (c) Preliminary segmentation: (a) a user-selected ROI; (b) edges of segmented layers; and (c) the fitted outer retinal contour, superimposed on the SOCT tomogram. (d) and (e) Final segmentation on the flattened and cropped SOCT tomogram: (d) a user-selected ROI and (e) edges of segmented layer.

smoothness of the approximated edge $L(x)$. If there is no information about the position of the edge $L(x)$ for a given x, the weight is set to zero. This procedure ensures that distortions and detachments in the retina have little impact on the shape of the fit. We calculate the smoothness as the inverse of the local variance $VL(x)$ of the edge position:

$$VL(x) = [L(x) - \tilde{L}(x)]^2 \otimes G(x), \tag{8}$$

where $G(x)$ is Gaussian kernel, and $\tilde{L}(x)$ is the local mean of the edge position:

$$\tilde{L}(x) = L(x) \otimes G(x). \tag{9}$$

In order to improve computation speed, convolution $\otimes$ is performed via FFT. The variance of $G(x)$ is chosen experimentally and is constant for images from the same instrument using the same measurement protocol.

In the following step, the automated flattening procedure is applied. Each A-scan of the 3-D set is shifted to ensure that the curved surface formed by all ORCs becomes a plane and that the resulting tomograms exhibit flat outer layers.

The signal from strongly reflective NFL interferes sometimes with the segmentation procedure. Therefore, before the second step, a mask that removes NFL and blood vessels is applied to all tomograms in the 3-D set [Fig. 5(d)]. Specific parameters characterizing the mask are adjusted by the operator for each case separately.

The final step involves applying the segmentation algorithm again, with the parameters σ_x and σ_z [Eq. (3)] chosen to be narrower than in the initial segmentation step. Now the segmentation lines adhere closer to highly scattering layers. This effect is inherent to the segmentation method since the region of interest is convolved with the Gaussian kernel $G(x,z)$ [Eq. (1)]. This second segmentation is also performed with the choice of a single ROI and visual evaluation of segmentation performance [Fig. 5(d) and 5(e)]. It is possible either to use the same ROI for both iterative steps or to choose manually another ROI if the visual evaluation done by the operator is not satisfying. Once chosen, the ROI is used for automated segmentation of the entire set of 3-D data, using a procedure that simultaneously divides the posterior and anterior parts of the contour into lines representing the basal part of the RPE and the IS/OS junction, respectively. The basal part of the RPE is the junction of RPE, Bruchs membrane and choriocappilaris. The entire processing procedure generates one set of three contours per tomogram: the RPE, the IS/OS junction and the ORC [Fig. 5(d) and 5(e)], which can be analyzed with respect to each other and the results displayed as

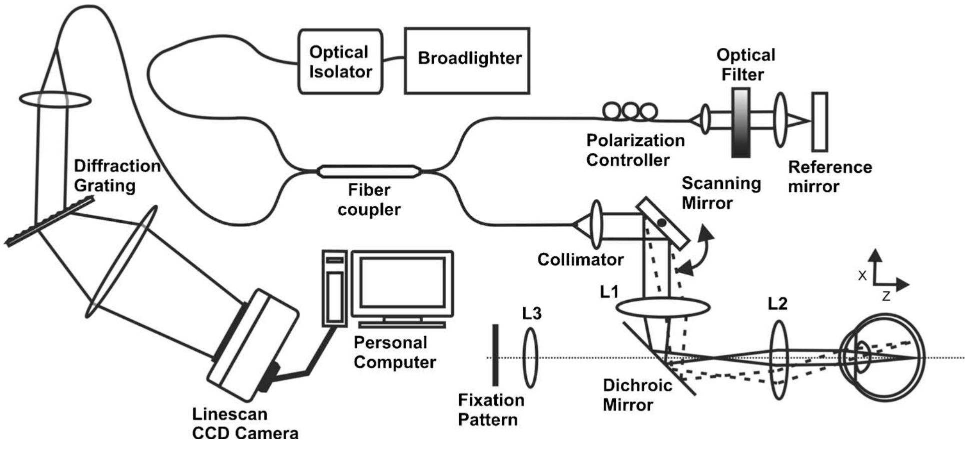

Fig. 6 Schematic drawing of the SOCT instrument.

contour maps in pseudo-color scale (shown later in Figs. 9 and 11).

3 Spectral OCT Instrument

The OCT data presented in this manuscript were obtained with a prototype SOCT instrument constructed at the Nicolaus Copernicus University. The instrument is optimized for use in the clinic. It enables acquisition of 25,000 axial lines (A-scans) per second preserving a high sensitivity of 95 dB. The schematic of the SOCT system is shown in Fig. 6. In order to achieve high axial resolution (4.5 μm), imaging is performed using a broadband light source (Broadlighter D830, Superlum, Moscow), centered at 830 nm, of 70-nm full width half maximum (FWHM). The light is coupled via an optical isolator (AC Photonics) to the Michelson interferometer, where it is split into reference and object arms. The Michelson interferometer is based on single-mode fibers with a broadband optical fiber coupler (AC Photonics). The light beam in the reference arm is attenuated by a neutral density filter and reflected back from the stationary reference mirror. The sample arm is terminated by the optical scan head, which enables the probe beam to be scanned on the retina in two lateral directions. In these experiments, a collimating lens of focal length $f_{col}=19$ mm, and a pair of lenses L1 ($f_{L1}=75$ mm) and L2 ($f_{L2}=30$ mm) were used to generate a beam incident on the cornea with a diameter of 0.8 mm at FWHM and focused onto the retina by the natural optics of the human eye. To ensure nonmydriatic operation of the OCT instrument, the galvanometric scanners (CamTech) are placed in the focal plane of lens L1, and the pupil of the eye is aligned to the focal plane of lens L2. In order to correct for the variation in refraction of the eye, the lens L2 is mounted with an axially adjustable mechanical translator. For an ideal natural optical eye system approximated by a single lens of 22.2 mm focal length, and assuming monochromatic radiation, the calculated transverse resolution is 10 μm. The experimentally estimated transverse resolution may be as high as 20 μm, whereas FOV is found to be approximately 6 mm. Both parameters strongly depend on the quality of the optics of the eye.

An additional dichroic mirror placed between lenses L1 and L2 enables the introduction of an internal fixation pattern consisting of three geometrical figures (cross, square, and circle), for measurements of the macula and the optic discs of the left and right eyes, respectively. The fixation pattern, including a background white light, is projected onto the retina through lenses L2 and L3. The entire interferometer, together with the scanning system, is mounted on an adjustable ophthalmic stand. The light beams returning from the reference mirror and from the sample are interfered at the output of the interferometer and analyzed by a spectrometer detection unit.

The detection unit is a custom-built spectrometer consisting of a high-speed, 12-bit A/D resolution, 2048-pixel CCD line-scan camera (Atmel) and a highly efficient volume holographic grating (Wasatch Photonics) with 1200 lines/mm and more than 80% first-order diffraction efficiency. The acquisition process and scanning protocols are controlled by a custom-designed compact electronic driving unit. The optical power incident on the eye is 750 μW, consistent with commercial OCT instruments and ANSI safety standards.[28,29]

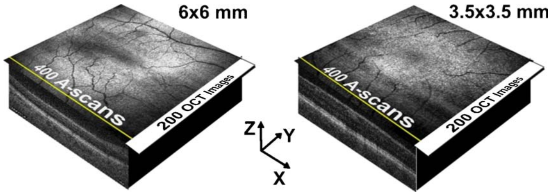

Fig. 7 Scanning protocols implemented to obtain lower scanning density; data suitable for quantitative, 3-D analysis. 200 cross-sectional images, each consisting of 400 A-scans: (left) transverse scanning range of 6×6 mm and (right) transverse scanning range of 3.5 ×3.5 mm.

In order to collect data suitable for clinical retinal imaging applications, we implemented four different scanning protocols for imaging each eye. It is important to obtain and analyze both standard, high-quality OCT cross-sectional images and quantitative contour maps, necessarily of lower resolution. To this end, two of the scanning protocols were designed to obtain high-quality (higher density of transverse scans) cross-sectional images and the other two to obtain lower transverse scan density, 3-D data suitable for quantitative analysis.

The scanning protocols are shown schematically in Figs. 7 and 8. For 3-D imaging (Fig. 7), both scanning protocols measure the same number (200) of cross-sectional images, each consisting of 400 A-scans with different transverse pixel density. The first transverse scanning range covers a macular area of 6×6 mm [Fig. 7(a)]. The segmentation procedure is extremely sensitive to changes of backscattering intensity, and in some cases, in eyes with ocular opacities or strong aberrations, the effective transverse field of view needed for segmentation was smaller than 6 mm. Typically, we crop our 3-D data set and display contour maps in a region of 5×5 mm since the rest of the region of interest is vignetted in an average number of cases. A second scanning protocol [Fig. 7(b)], enabling 3-D OCT data collection over a square area of 3.5 ×3.5 mm was chosen to visualize small pathological changes. Higher sampling density also helps to increase the OCT signal[8] and is very useful in the cases with significant ocular media opacities such as in early cataracts. Both scanning protocols are performed within 3 s and enable dense coverage of the retina. For the 6×6 mm scanning pattern, the spacing is 30/15 μm in the superior-inferior/temporal-nasal direction. For the 3.5×3.5 mm scanning pattern, the spacings are 18/9 μm in the superior-inferior/temporal-nasal direction.

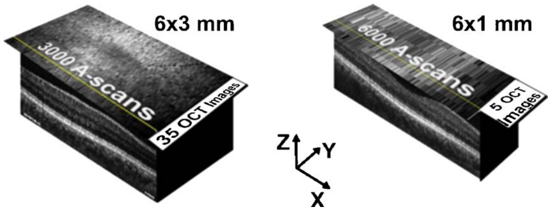

Fig. 8 Scanning protocols implemented to obtain higher scanning density; data suitable for qualitative analysis. (Left) 35 cross-sectional images, each consisting of 3,000 A-scans; transverse scanning range of 6×3 mm. (Right) one cross-sectional image, consisting of 6,000 A-scans; transverse scanning length of 6×1 mm.

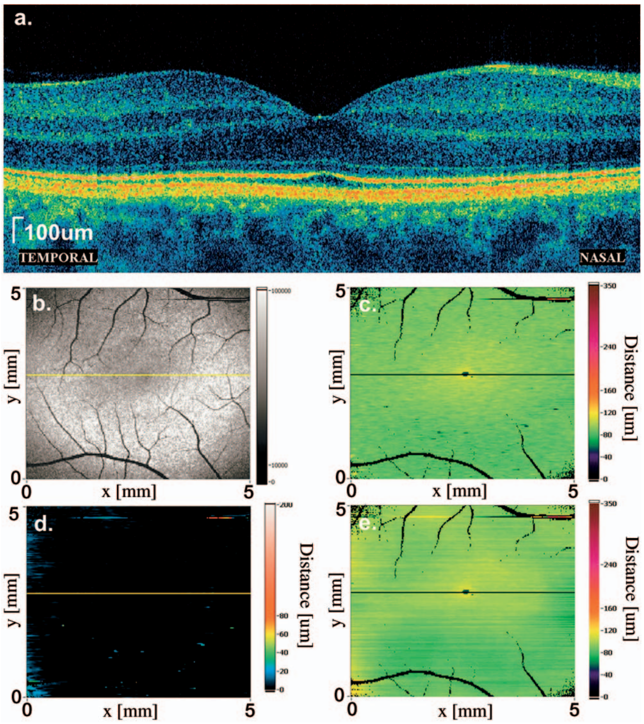

Fig. 9 Analysis of SOCT data for the macular region of a normal (right) eye. (a) High-quality cross-sectional SOCT image (6,000 A-scans) and (b) SOCT fundus image. (c) to (e) Contour maps representing the thickness between: (c) posterior part of the RPE and IS/OS junction; (d) posterior part of the RPE and the outer retinal contour; and (e) IS/OS junction and outer retinal contour.

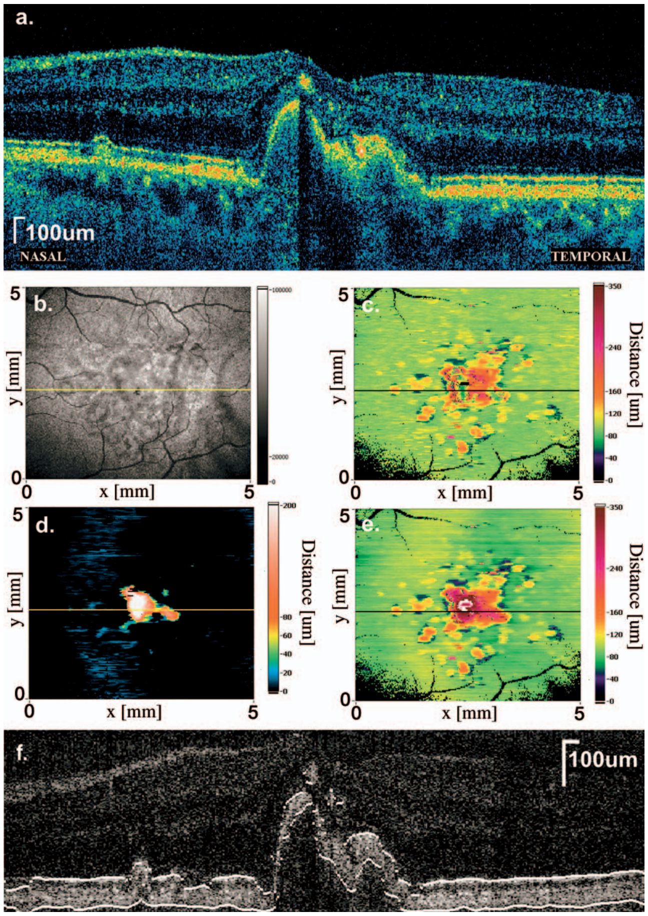

Fig. 10 Analysis of SOCT data for the macular region of the (left) eye of a patient with age-related macular degeneration. (a) High-quality cross-sectional SOCT image (3,000 A-scans) and (b) SOCT fundus image. (c) to (e) Contour maps representing the thickness between: (c) posterior part of the RPE and IS/OS junction; (d) posterior part of the RPE and the outer retinal contour; and (e) IS/OS junction and outer retinal contour. (f) Single cross-sectional image from the set of 3-D data used for creation of thickness maps with a segmented IS/OS–RPE layer complex.

The two scanning protocols used for qualitative analysis are shown schematically in Fig. 8. In order to collect general information about structural changes of the retina caused by pathology, 35 cross-sectional images, each consisting of 3,000 A-scans, covering an area of 6×3 mm were acquired [Fig. 8(a)]. The total measurement time for this protocol is less than 4 s. The scanning protocol, shown schematically in Fig. 8(b), is used to maximally enhance the image quality and sensitivity of the OCT measurements. In a limited number of cases, the opacity of the eye is high enough to severely reduce the signal in the OCT image. Using five OCT images each consisting of 6,000 A-scans, one can improve the image quality significantly, and a more detailed retinal structure can be revealed. This protocol has the trade-off that a smaller area of the fundus is covered. The measurement time using this scanning protocol is one second. Raster scanning is performed in all protocols to facilitate reconstruction of the fundus image. The data are stored in raw digital form and analyzed after the measurement session.

4 Results

In order to test the performance of the segmentation and mapping method, OCT data from normal eyes and eyes with a selection of retinal pathologies were processed. Figures 9–11 show three examples of quantitative analysis of outer retinal layers. Figure 9(a) shows a high-quality SOCT cross-sectional image (6,000 A-scans covering 6 mm in the temporal-nasal direction) of the macula of a normal eye. The most highly scattering outer retinal layers, including the junction between the inner and outer segments of the photoreceptor layer (IS/OS) and RPE are clearly distinguishable and separated from each other. Figure 9(b) shows the SOCT fundus view reconstructed from 3-D OCT data acquired in the same eye.

The position of the high-quality OCT cross-sectional image [Fig. 9(a)] is marked on the fundus image and contour maps by the yellow and black cursor lines. This image was registered with cross-sectional images from the set of 3-D data, which are used to construct the fundus view and contour maps. The contour map of distances between the IS/OS junction and the posterior part of the RPE is shown in Fig. 9(c). In the normal eye, the thickness of this layer is uniform throughout almost the entire 5×5 mm area of the fundus. Only in close proximity to the central foveal pit the distance between the IS/OS junction and RPE become thicker. In this range, we often also observe a small drop in the reflectivity of the IS/OS junction, causing a small depression visible in the central part of the contour maps. Since the normal retina is smooth and continuous, contour maps representing distances from the

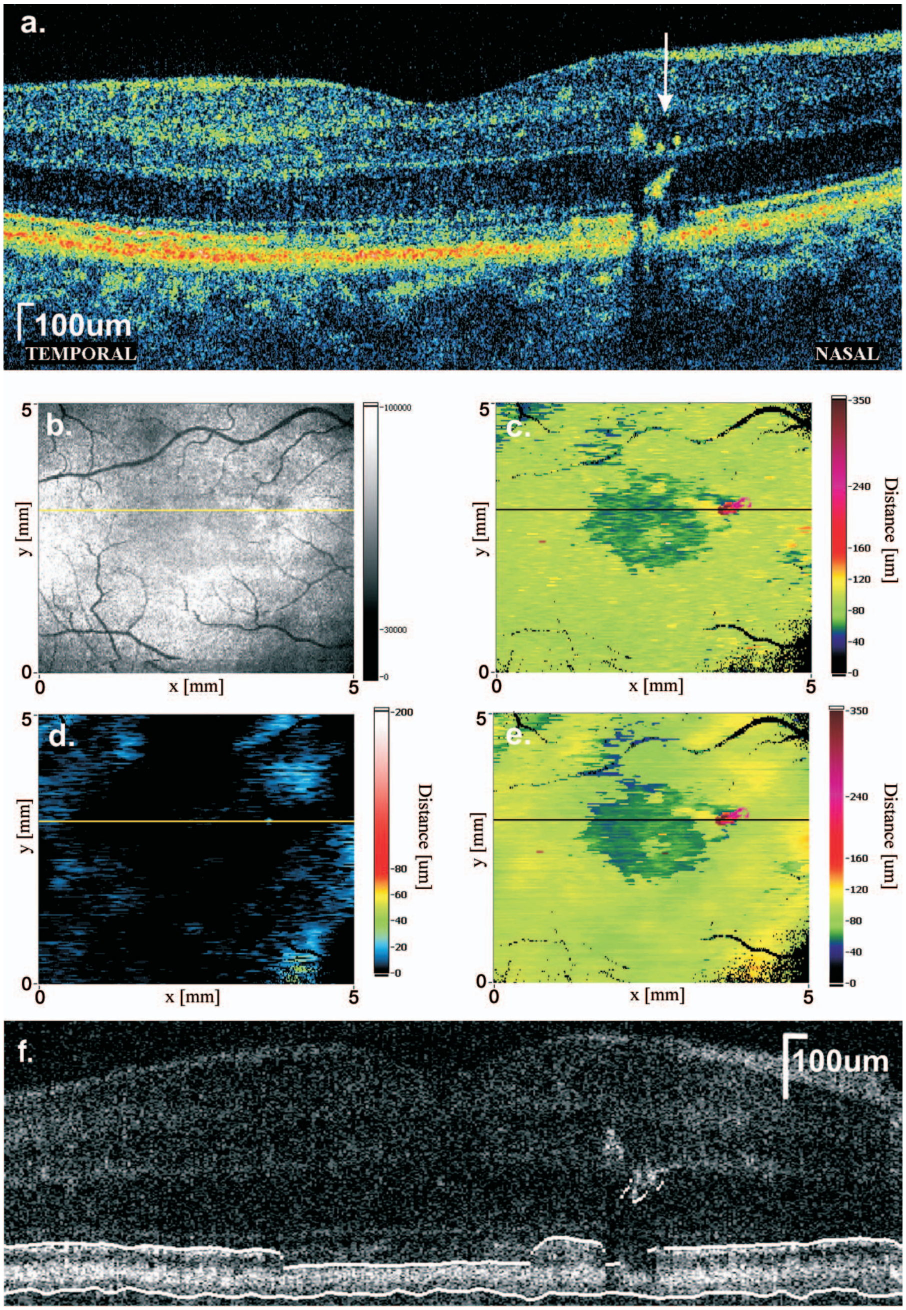

Fig. 11 Analysis of SOCT data for the macular region of the fellow (right) eye of a patient suffering from idiopathic cystoid macular edema (a) High-quality cross-sectional SOCT image (3,000 A-scans), white arrow indicates pigment deposits and (b) SOCT fundus image. (c) to (e) Contour maps representing the thickness between: (c) posterior part of the RPE and IS/OS junction; (d) posterior part of the RPE and the outer retinal contour; and (e) IS/OS junction and the outer retinal contour. (f) Single cross-sectional image from the set of 3-D data used for creation of thickness maps with a segmented IS/OS–RPE layer complex.

RPE to the ORC and from the IS/OS junction to the ORC [Fig. 9(d) and 9(e)] do not provide any additional information.

The IS/OS junction to ORC and RPE to ORC distance maps are dramatically different for SOCT data obtained from the eye of a patient with wet age-related macular degeneration (wet AMD), as presented in Fig. 10. The transverse distribution of the central elevation of the RPE, caused by confluent drusen visible in high-quality cross-sectional images [Fig. 10(a)] is clearly seen in both the ORC to RPE and ORC to IS/OS junction thickness maps. A side effect of RPE elevation is a decrease in the IS/OS junction reflectivity, clearly visible in OCT images. This may be related either to the partial atrophy of photoreceptors and/or to structural changes in photoreceptors. In that case, the map of distances from the RPE to the IS/OS junction does not reveal the entire extent of retinal changes, and further comparison with IS/OS junction to ORC and RPE to ORC maps is needed. The RPE to ORC contour map [Fig. 10(d)] enables delineation of the area of RPE elevation. The IS/OS junction to ORC contour map [Fig. 10(e)] enables the identification of drusen distribution. Again, the low-frequency irregularities caused by mismatch between the real retinal shape and the parabolic fit to the ORC are visible in the IS/OS junction to ORC and RPE to ORC maps.

In some pathological changes, a decrease in IS/OS junction reflectivity is observed. This decrease can also be mapped using the method of segmentation and analysis of outer retinal layers. Figure 11 shows a high-quality cross-sectional SOCT image and the contour maps calculated from SOCT data for a patient successfully treated for idiopathic cystoid macular edema (CME). Most of the changes disappeared in both eyes; however, small cysts in internal retinal layers still can be observed. In SOCT cross-sectional images of the right eye [Fig. 11(a)] there is also a significant drop in IS/OS junction reflectivity. The region of decreased reflectivity can be found and delineated by using either the IS/OS junction to RPE or the IS/OS junction to ORC maps [Fig. 11(c) and 11(e)]. The presence of a very small focal change localized nasally to the fovea is also delineated, and this small disruption is visible on the RPE to ORC map as well [Fig. 11(d)]. This highly scattering lesion probably corresponds to pigment deposits visible also by the standard ophthalmoscopy.

5 Discussion

The method of segmentation used in this study identifies regions in the tomogram that have similar intensity and variance. This causes some artifacts in the resulting thickness maps. One of the major artifacts is the simultaneous segmentation of RPE–IS OS complex along with other parts of the retina. Sometimes NFL pixels are assigned to the same category as pixels of RPE–IS OS [Fig. 5(b) and 5(c)]. In this case, because the location of the NFL is well defined, we can use a suitable mask that effectively removes the NFL from the image [Fig. 5(d) and 5(e)]. Another artifact of that kind is shown in Fig. 11 (white arrow). The deposits of pigment situated above the RPE are included by the algorithm to the RPE–IS OS complex. This is an erroneous classification, which gives rise to an incorrect value for the complex thickness. However, such errors are inherent to many segmentation techniques due to the complexity of morphological changes caused by the pathologies. Nevertheless, the resulting map indicates regions of the retina that require further attention [dark-red regions in Fig. 11(c) and 11(e)]. By additional examination of corresponding cross-sectional images, the clinician may decide unequivocally the real nature of the thickness change [Fig. 11(a) and 11(f)].

Drops in intensities of tomogram pixels lead to other kinds of artifacts. These can occur when the reflectivity of RPE decreases due to pathological processes. Such a case is plotted in Fig. 11. The resulting thickness map reveals the areas affected with the disease [darker regions in the center of the thickness maps, Fig. 11(c) and 11(e)]. In this case, the so-called artifact provides useful information about the disease and can be also used as a marker for early pathologic changes in the future. Unfortunately, similar effects arise from intensity drops connected with the gradual fading of the signal toward the edges of the transversal field of view (FOV). This artifact causes thickness maps to show thinning of the retina in proximity of the edges of the imaged area of the retina. An inhomogeneous distribution of backscattered light in the SOCT fundus image also indicates the transverse FOV. The brightly scattering doughnut shape visible in fundus views corresponds to the region where the focal plane intercepts the retina within the range of depth of focus. The impact of these artifacts can be reduced by marking the areas on the thickness maps where the thickness is very low and therefore is assessed with uncertainty. In practice, this is done by assigning zero [black on the edges of color maps in Figs. 9 to 11(c) and 11(e)] to regions where the corresponding fundus view drops below a certain threshold. A similar artifact that is observed in almost all segmentations is caused by a drop of reflectivity of the IS/OS junction in the center of the fovea [darker spot in the center of the thickness maps, Fig. 9(c) and 9(e)]. As result, thinning or even a small hole in the RPE–IS OS complex is observed. Unfortunately, this artifact cannot be compensated with our method.

The present version of the software was written in LabView. The calculations for the segmentation process take approximately 700 ms per tomogram (composed of 400 transverse pixels and 600 axial pixels) for the first segmentation and 250 ms for the second using cropped data. The calculations are performed on a personal computer with a Pentium 4, 2 GHz processor. Full processing of a data set consisting of 200 images, generating all three contour maps, takes approximately 3 min. Including manual intervention, the entire time taken was approximately 5 min. This time can be significantly shortened using a more efficient programming environment.

In general, our processing can be iterated multiple times with multiple carefully chosen ROIs. For example, if the scanning protocol is not optimized with respect to the transverse FOV, then the pixel properties within the layer change slightly from tomogram to tomogram, and from the center of the tomogram to its edge. This makes it necessary to choose multiple ROIs from different parts of the tomograms in order to properly construct the function approximating the cluster containing the majority of points in the layer. A proper choice of the scanning protocol with respect to the specifications of the SOCT instrument and focusing on layers of similar properties will decrease the need for manual intervention and increase the accuracy of the segmentation procedure.

Reducing the need for manual intervention can be also useful for further enhancement of performance and reliability of the overall processing. In principle, it is possible to introduce a fully automated method of indicating the ROI, since the highly scattering posterior retinal layers are easily distinguishable from the other retinal layers.

However, the complexity of morphological changes caused in the retinal layers by retinal pathologies can be severe. Therefore, in order to establish reliable automated algorithms, further studies, including investigating the performance of the algorithm on different retinal pathologies, are needed.

6 Conclusions

We have presented a method of segmentation and analysis of posterior retinal layers using high-speed SOCT. We optimized the performance of the ophthalmic SOCT prototype and the scanning protocols. An algorithm and a method for layer segmentation and visualization of contour thickness maps was demonstrated. We also demonstrated the use of the ORC, which creates a reference plane for analysis and corresponds to the smooth, healthy retinal shape. The first results showing quantitative analysis of posterior retinal layers in normal and retinal pathology cases were demonstrated. We believe that this method will extend the usefulness of SOCT due to a better interpretation of the data and provide a better understanding of disease pathogenesis as well as more sensitive diagnostic indicators of early disease progression.

Acknowledgments

This work was supported by the Polish Ministry of Science and Higher Education, grants for years 2006/2008. J. Fujimoto receives royalties from intellectual property licensed from MIT to Carl Zeiss Meditec. Maciej Wojtkowski acknowledges the additional support of the Foundation for Polish Science (Homing Project) and the Rector of Nicolaus Copernicus University (504-F).

References

1. D. Huang, E. A. Swanson, C. P. Lin, J. S. Schuman, W. G. Stinson, W. Chang, M. R. Hee, T. Flotte, K. Gregory, C. A. Puliafito, and J. G. Fujimoto, "Optical coherence tomography," *Science* **254**(5035), 1178–1181 (1991).
2. J. G. Fujimoto, M. E. Brezinski, G. J. Tearney, S. A. Boppart, B. Bouma, M. R. Hee, J. F. Southern, and E. A. Swanson, "Optical biopsy and imaging using optical coherence tomography," *Nat. Med.* **1**(9), 970–972 (1995).
3. W. Drexler, U. Morgner, R. K. Ghanta, F. X. Kärtner, J. S. Schuman, and J. G. Fujimoto, "Ultrahigh-resolution ophthalmic optical coherence tomography," *Nat. Med.* **7**(4), 502–507 (2001).
4. A. F. Fercher, C. K. Hitzenberger, G. Kamp, and S. Y. Elzaiat, "Measurement of intraocular distances by backscattering spectral interferometry," *Opt. Commun.* **117**(1–2), 43–48 (1995).
5. M. Wojtkowski, R. Leitgeb, A. Kowalczyk, T. Bajraszewski, and A. F. Fercher, "*In vivo* human retinal imaging by Fourier domain optical coherence tomography," *J. Biomed. Opt.* **7**(3), 457–463 (2002).
6. M. Wojtkowski, V. Srinivasan, J. G. Fujimoto, T. Ko, J. S. Schuman, A. Kowalczyk, and J. S. Duker, "Three-dimensional retinal imaging with high-speed ultrahigh-resolution optical coherence tomography," *Ophthalmology (Philadelphia)* **112**(10), 1734–1746 (2005).
7. M. Wojtkowski, T. Bajraszewski, I. Gorczynska, P. Targowski, A. Kowalczyk, W. Wasilewski, and C. Radzewicz, "Ophthalmic imaging by spectral optical coherence tomography," *Am. J. Ophthalmol.* **138**(3), 412–419 (2004).
8. M. Wojtkowski, V. J. Srinivasan, T. H. Ko, J. G. Fujimoto, A. Kowalczyk, and J. S. Duker, "Ultrahigh-resolution, high-speed, Fourier domain optical coherence tomography and methods for dispersion compensation," *Opt. Express* **12**(11), 2404–2422 (2004).
9. B. J. Kaluzny, J. J. Kaluzny, A. Szkulmowska, I. Gorczynska, M. Szkulmowski, T. Bajraszewski, P. Targowski, and M. Wojtkowski, "Spectral optical coherence tomography: a novel technique for cornea imaging," *Cornea* (in press, 2006).
10. R. A. Costa, M. Skaf, L. A. Melo Jr., D. Calucci, J. A. Cardillo, J. C. Castro, D. Huang, and M. Wojtkowski, "Retinal assessment using optical coherence tomography," *Prog. Retin Eye Res.* **25**(3), 325–353 (2006).
11. U. Schmidt-Erfurth, R. A. Leitgeb, S. Michels, B. Povazay, S. Sacu, B. Hermann, C. Ahlers, H. Sattmann, C. Scholda, A. F. Fercher, and W. Drexler, "Three-dimensional ultrahigh-resolution optical coherence tomography of macular diseases," *Invest. Ophthalmol. Visual Sci.* **46**(9), 3393–3402 (2005).
12. B. J. Kaluzny, J. J. Kaluzny, A. Szkulmowska, I. Gorczynska, M. Szkulmowski, T. Bajraszewski, P. Targowski, and A. Kowalczyk, "Spectral optical coherence tomography: a new imaging technique in contact lens practice," *Ophthalmic Physiol. Opt.* **26**(2), 127–132 (2006).
13. N. A. Nassif, B. Cense, B. H. Park, M. C. Pierce, S. H. Yun, B. E. Bouma, G. J. Tearney, T. C. Chen, and J. F. de Boer, "*In vivo* high-resolution video-rate spectral-domain optical coherence tomography of the human retina and optic nerve," *Opt. Express* **12**(3), 367–376 (2004).
14. B. Cense, N. A. Nassif, T. C. Chen, M. C. Pierce, S.-H. Yun, B. H. Park, B. E. Bouma, G. J. Tearney, and J. F. de Boer, "Ultrahigh-resolution high-speed retinal imaging using spectral-domain optical coherence tomography," *Opt. Express* **12**(11), 2435–2447 (2004).
15. M. Szkulmowski, A. Wojtkowski, T. Bajraszewski, I. Gorczynska, P. Targowski, W. Wasilewski, A. Kowalczyk, and C. Radzewicz, "Quality improvement for high resolution *in vivo* images by spectral domain optical coherence tomography with supercontinuum source," *Opt. Commun.* **246**(4–6), 569–578 (2005).
16. W. Drexler, "Ultrahigh-resolution optical coherence tomography," *J. Biomed. Opt.* **9**(1), 47–74 (2004).
17. C. A. Toth, D. G. Narayan, S. A. Boppart, M. R. Hee, J. G. Fujimoto, R. Birngruber, C. P. Cain, C. D. DiCarlo, and W. P. Roach, "A comparison of retinal morphology viewed by optical coherence tomography and by light microscopy," *Arch. Ophthalmol. (Chicago)* **115**(11), 1425–1428 (1997).
18. M. Gloesmann, B. Hermann, C. Schubert, H. Sattmann, P. K. Ahnelt, and W. Drexler, "Histologic correlation of pig retina radial stratification with ultrahigh-resolution optical coherence tomography," *Invest. Ophthalmol. Visual Sci.* **44**(4), 1696–1703 (2003).
19. W. Drexler, H. Sattmann, B. Hermann, T. H. Ko, M. Stur, A. Unterhuber, C. Scholda, O. Findl, M. Wirtitsch, J. G. Fujimoto, and A. F. Fercher, "Enhanced visualization of macular pathology with the use of ultrahigh-resolution optical coherence tomography," *Arch. Ophthalmol. (Chicago)* **121**(5), 695–706 (2003).
20. D. Koozekanani, C. Roberts, S. E. Katz, and E. E. Herderick, "Intersession repeatability of macular thickness measurements with the Humphrey 2000 OCT," *Invest. Ophthalmol. Visual Sci.* **41**(6), 1486–1491 (2000).
21. D. Koozekanani, K. Boyer, and C. Roberts, "Retinal thickness measurements from optical coherence tomography using a Markov boundary model," *IEEE Trans. Med. Imaging* **20**(9), 900–916 (2001).
22. H. Ishikawa, D. M. Stein, G. Wollstein, S. Beaton, J. G. Fujimoto, and J. S. Schuman, "Macular segmentation with optical coherence tomography," *Invest. Ophthalmol. Visual Sci.* **46**(6), 2012–2017 (2005).
23. D. C. Fernandez, H. M. Salinas, and C. A. Puliafito, "Automated detection of retinal layer structures on optical coherence tomography images," *Opt. Express* **13**(25), 10200–10216 (2005).
24. D. C. Fernandez, "Delineating fluid-filled region boundaries in optical coherence tomography images of the retina," *IEEE Trans. Med. Imaging* **24**(8), 929–945 (2005).
25. M. Mujat, R. Chan, B. Cense, B. Park, C. Joo, T. Akkin, T. Chen, and J. de Boer, "Retinal nerve fiber layer thickness map determined from optical coherence tomography images," *Opt. Express* **13**(23), 9480–9491 (2005).
26. J. C. Russ, *The Image Processing Handbook*, CRC Press (2002).
27. A. R. Weeks, *The Fundamentals of Electronic Image Processing*, SPIE Press and IEEE Press (1996).
28. "American national standard for safe use of lasers," A.N.S. Institute (2000).
29. "Polskie Normy," Wydawnictwo Normalizacyjne Alfa (1992).